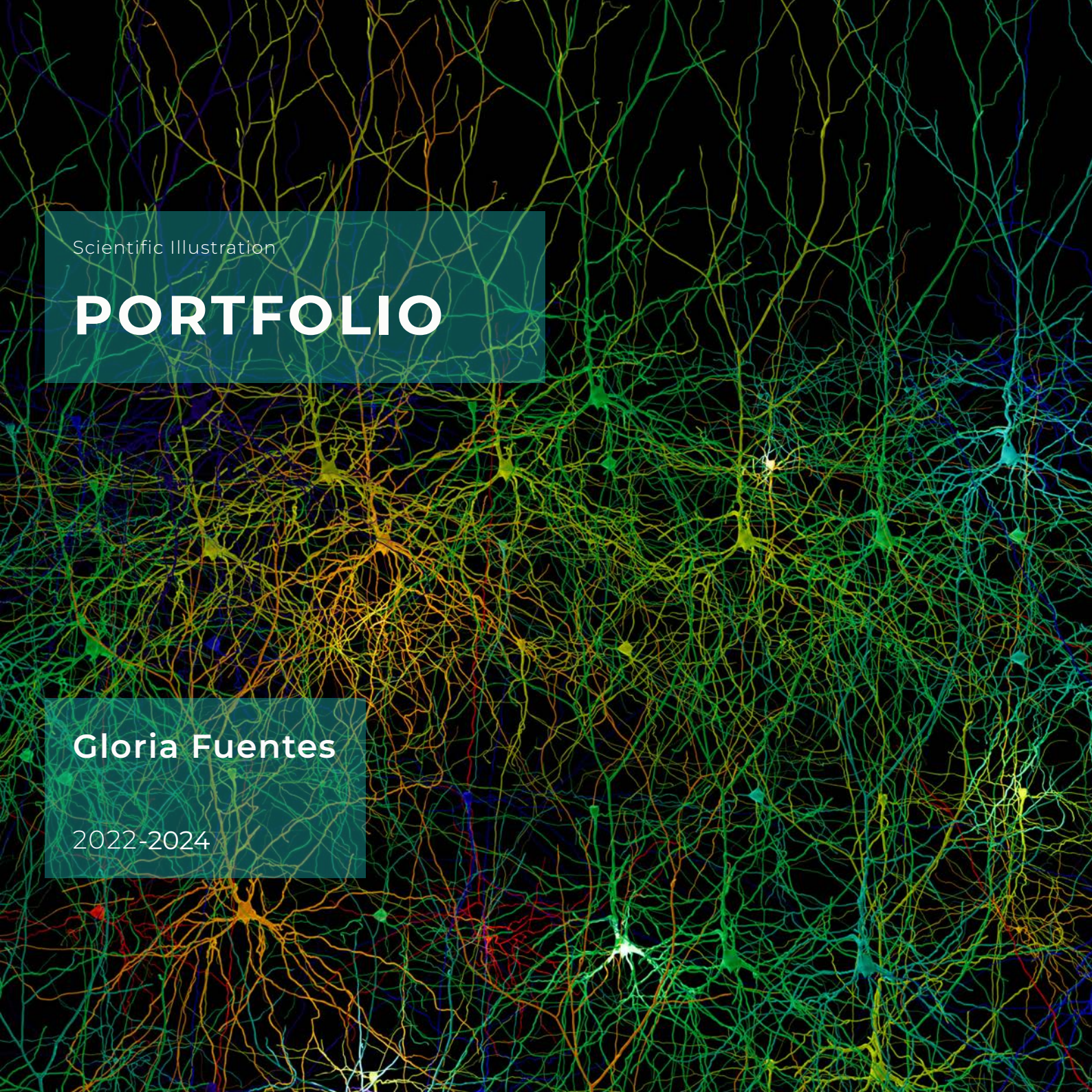

Scientific Illustration

PORTFOLIO

Gloria Fuentes

2022-2024

My name is Gloria, and I am a Visual Thinker and communicator with over 20 years of experience in computational and biomedical research. My strength lies in organising and conveying complex information visually.

In this new venture, I am merging my scientific analytical skills with professional art design to develop visual campaigns that present intricate projects with the perfect blend of accuracy and visual appeal.

My lifelong goal is continually enhancing my skills while learning new ones in Illustration and Animation. I aspire to be an eternal student, keeping my mind engaged well into old age.

Let's unleash creativity to bridge the gap between Science and Society: "If I can illustrate it, you can understand it."

EDUCATION

Doctorate	Ph.D. Molecular Biology
Master	Postgraduate Certificate in Education
Master	Scientific Illustration (Academia Trazos)
Master	3D Animation (Academia Trazos)
Degree	B. Sc. Chemical Sciences

OTHER RELEVANT COURSES

S.P.A.R.K. | 5 strategies for the visual communication of science

Infographics and Data Visualization. 5W Academy.

Curso de infografía. Ciencia a la vista. Fundamentium School.

Design Graduate - UI/UX. Instituto Tramontana.

Presentation Skills. Ludens Seminar & Private Coaching.

PROFESSIONAL SKILLS

- Adobe Illustrator
- Adobe Photoshop
- Adobe InDesign
- Adobe Lightroom
- Zbrush
- Cinema 4D
- Adobe After Effects

- Graphical macromolecule representation packages- Pymol, Chimera, VMD
- Molecular simulation packages
- Macromolecular docking packages
- Scripting languages
- Writing and edition of scientific papers & grants
- Data Manipulation & Visualization
- Analytical thinking

TIMELINE

1997 — **B. Sc. in Chemical Sciences, University of Extremadura. Spain.**

1998 — **Predoctoral Fellow.**
Instituto de Cataliísis y Petroleoquímica (CSIC), Madrid. Spain.

2002 — **Ph.D. (Molecular Biology Department), Autonoma University, Madrid. Spain.**

2003 — **Postdoctoral Fellow.**
NMR Spectroscopy Department, Utrecht University. The Netherlands.

2006 — **Visiting Scientist.**
Bioinformatics Unit,Centre for Molecular Biology "Severo Ochoa" (CMBSO), Madrid. Spain.

2007 — **Staff scientist.**
Structural and Computational Biology, Spanish National Cancer Research Centre, Madrid. Spain.

2009 — **Senior Research Fellow.**
Bioinformatics Institute, A*STAR, Singapore.

2011 — **Assistant Principal Investigator.**
Bioinformatics Institute, A*STAR, Singapore.

2013 — **Research Scientist.**
Structure-based Molecular Design Team, RIKEN Center for Life Science Technologies, Yokohama, Japan.

2016 — **Head of Computational & Structural Biology.**
Hummingbird Bioscience. Singapore.

2017 — **Freelance Scientific Illustrator & Animator.**
The Visual Thinker, Singapore. West Hartford, CT. USA.

2022 — **Contractor - Communications & Marketing.**
The Jackson Laboratory. Farmington, CT. USA.

2024 — **Scientific Illustrator**
Life Science Editors, NL & USA. KAUST, Saudi Arabia.

MEMBERSHIPS

SEBBM

SEBiBC
Sociedad Española de Bioinformática y Biología Computacional

Professional Member
American Medical Illustrators
2020

GMS

ASC

MARIE CURIE ALUMNI

ASBMB

SELECTED SCIENTIFIC PUBLICATIONS

h-index: 16

G. Fuentes and A. Valencia. **Classical effectors of Ras: New tales from in silico complexes.** Trends in Biochem Sci, 34(11):533-9. 2009.

A. Rojas, G. Fuentes, A. Rausell and A. Valencia. **The evolution of small GTPases in signaling.** Journal Cell Biology, 196:2, 189-201. 2012.

G. Fuentes, M. Scaltri , J. Baselga & C.S. Verma. **Synergy between trastuzumab and pertuzumab for Her2: in silico insights.** Breast Cancer Research, 13:3, R54. 2011.

ONLINE PROFILE

Linkedin

Twitter

www.thevisualthinker.xyz

SCIENTIFIC FIGURES

Pediatric Cancer Drug Development Pipeline

Client: The Jackson Laboratory
Year: 2023
Software: Adobe Photoshop - Adobe Illustrator

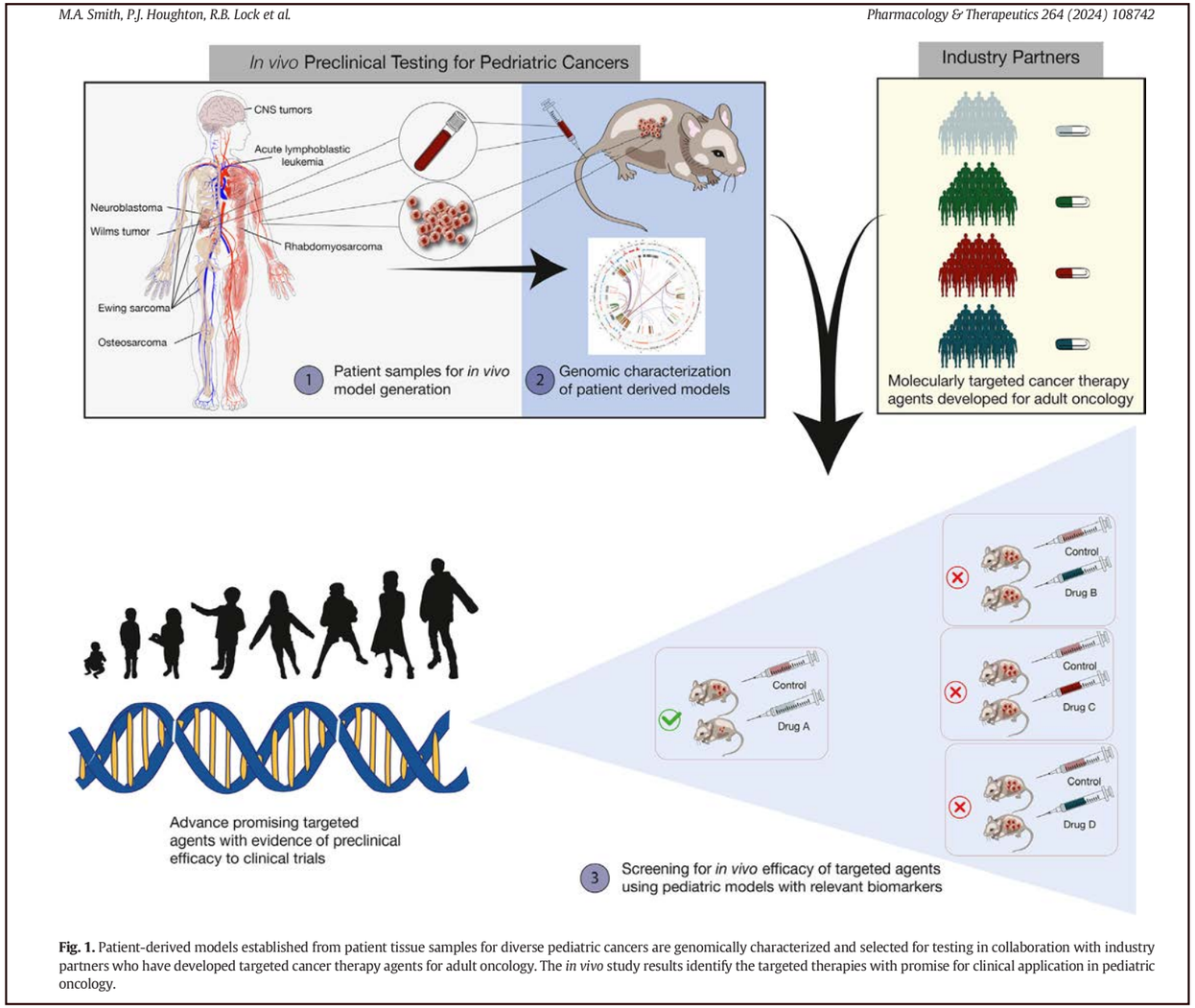

Fig. 1. Patient-derived models established from patient tissue samples for diverse pediatric cancers are genomically characterized and selected for testing in collaboration with industry partners who have developed targeted cancer therapy agents for adult oncology. The *in vivo* study results identify the targeted therapies with promise for clinical application in pediatric oncology.

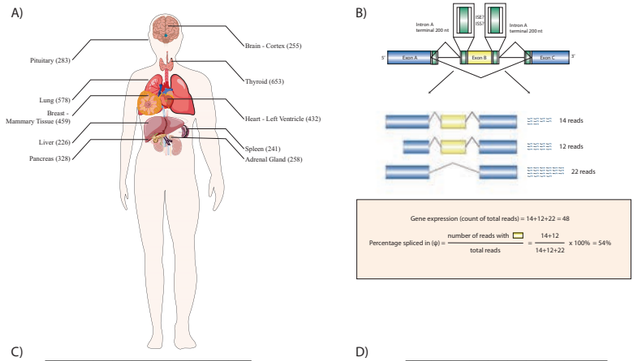

exons than genes containing only type 0 exons. The genes containing them had on average slightly fewer transcripts (13 and 12 for UHP and DHP, respectively, and 14 for type 0). Furthermore, type UHP/DHP exons are included in a larger proportion of transcripts than type 0 exons.

We define the "upstream" intron as the last contiguous non-coding region that is transcribed 5′ to the exon, and the "downstream" intron as the first such region that is transcribed 3′ to the exon. The median upstream intron lengths were 572 bp for types 0, 857 bp for type UHP, and 732 bp for DHP; the differences between UHP or DHP and type 0 were statistically

Multitissue RNA-seq analysis identifies association between gene expression

Client: The Jackson Laboratory
Year: 2023
Software: Adobe Photoshop - Adobe Illustrator

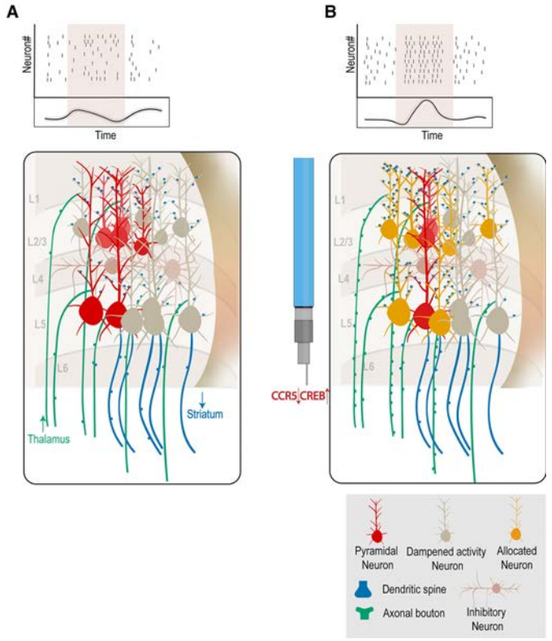

Figure 2. Functional allocation in neural circuits after stroke. ***A***, Stroke causes loss of connectivity and reduction in spiking activity and synchronization. Shaded region represents stroke. Red represents pyramidal neurons in layers 2/3 and 5 in peri-infarct cortex. Green represents inputs from the thalamus. Blue represents output to the striatum. Gray pyramidal neurons indicate those with dampened activity after stroke from loss of structural connectivity and reduction in spine densities and axonal boutons. Time series plot above represents reduction in movement-related spiking activity (shaded region) with the trace of the population average shown below. ***B***, Enhancing excitability within neuronal circuits either through neurostimulation (blue device on left) time-locked to task onset or with genetic modulations of CCR5 or CREB allows selective integration of excitable neurons into a functional motor circuit. Yellow represents allocated neurons. Functional allocation leads to restoring connectivity through increased spine densities, spiking activity, and synchronization.

2010). However, there is little direct evidence that IHI explains these findings, and there is also evidence that increased right-hemisphere activation may be compensatory and that its inhibition by experimental means or a second stroke is detrimental (Kinsbourne, 1971; Turkeltaub et al., 2012; Turkeltaub, 2015). Thus, as for motor recovery (Xu et al., 2019; Mirdamadi et al., 2023), the role of IHI in aphasia is still in question (Gainotti, 2015).

Another instance in which IHI has been proposed to play a role in stroke-induced disability is spatial neglect. Spatial neglect is characterized by asymmetric spatial performance (e.g., failure to detect or move toward stimuli on the contralesional side) that is not explained by a basic sensory or motor deficit, and it is more common, severe, and persistent after right-hemispheric injury (Stone et al., 1993; Ten Brink et al., 2017). It has been proposed that each hemisphere has a contralateral attention bias, and that the hemispheres inhibit one another through transcallosal IHI (Kinsbourne, 1970). Unilateral lesions may produce neglect of contralateral space because the damaged hemisphere is impaired both in its ability to direct attention to the contralesional side and in its ability to inhibit the opposing hemisphere's attentional bias toward the ipsilesional side. Neglect may be less severe and persistent after left-hemisphere lesions either because of the right hemisphere's dominant role for attention (Robertson et al., 1998; Husain and Rorden, 2003) and/or because the right hemisphere can allocate attention to both sides of space, which allows it to compensate for left-hemisphere lesions (Heilman and Van Den Abell, 1980; Mesulam, 1999). Support for the IHI hypothesis of spatial neglect includes a case study in which neglect caused by a right parietal lesion resolved after a second infarct to the left frontal cortex (Vuilleumier et al., 1996), functional neuroimaging evidence for a link between normalization

Neuronal circuit recovery after stroke

Client: The Jackson Laboratory
Year: 2023
Software: Adobe Illustrator

Mechanisms of TTN Variants in Dilated Cardiomyopathy

Client: The Jackson Laboratory
Year: 2023
Software: Adobe Photoshop - Adobe Illustrator

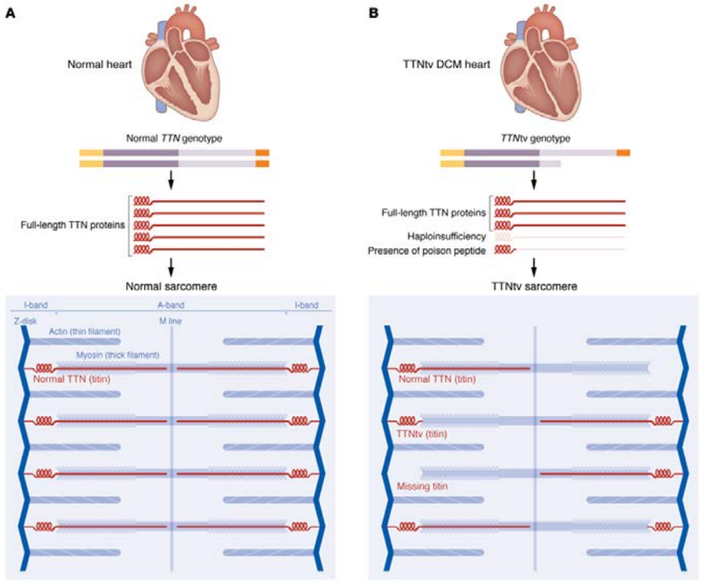

Figure 1. A dominant-negative or poison peptide model accounts for how some *TTN*tvs may contribute to DCM pathogenesis. Heterozygous *TTN*tvs are the most prevalent genetic lesion identified in DCM, but the disease mechanism remains elusive. Accumulating evidence shows that some TTNtvs integrate within the sarcomere and are load bearing. At the same time, TTNtvs are also shown to reduce the amount of full-length TTN protein (haploinsufficiency). At present, either mechanism remains a plausible driver of DCM, with the possibility that both contribute in tandem.

TTNtv proteins as well as full-length TTN protein haploinsufficiency. One such approach may be to combine human iPSC models and genome-editing technologies such as CRISPR. Despite maturation limitations, human iPSC–derived cardiomyocytes can be developed using CRISPR genetic ablation of truncated TTN protein to explore the specific functional impact of these poison peptides. Through the use of a 3D cardiac microtissue model to study sarcomere contractile function in a biomimetic context, truncated TTN ablation was shown to partially rescue sarcomere function, thus implicating truncated TTN as a sarcomere poison. Because the rescue was partial, this study also supported a combinatorial genetic mechanism including haploinsufficiency (19). Continued efforts toward a precise understanding of how TTNtvs lead to DCM and other cardiomyopathies will catalyze the development of mechanistically precise therapies targeting one of the most important heart failure causes in the field.

Acknowledgments

We thank Gloria Fuentes for assistance with figure design. Funding supported was obtained from the NIH (R01HL165220, to JTH and SGC).

Address correspondence to: J. Travis Hinson, The Jackson Laboratory for Genomic Medicine, 10 Discovery Lane, Farmington, Connecticut 06032, USA. Phone: 860.837.2048; Email: travis.hinson@jax.org.

1. LeWinter MM, Granzier H. Cardiac titin: a multifunctional giant. *Circulation*. 2010;121(19):2137–2145.
2. Zaunbrecher RJ, et al. Cronos titin is expressed in human cardiomyocytes and necessary for normal sarcomere function. *Circulation*. 2019;140(20):1647–1660.
3. Neagoe C, et al. Titin isoform switch in ischemic human heart disease. *Circulation*. 2002;106(11):1333–1341.
4. Lahmers S, et al. Developmental control of titin isoform expression and passive stiffness

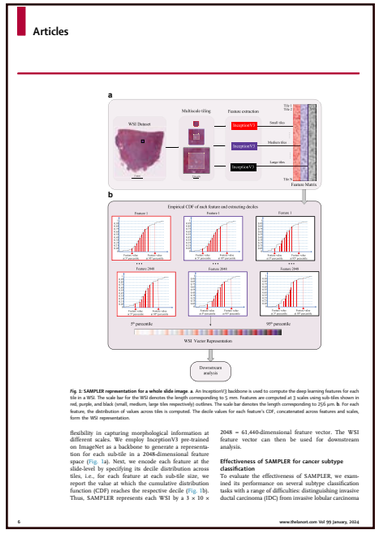

Fig. 1: SAMPLER representation for a whole slide image. a, An Inception*V3 backbone is used to compute the deep learning features for each tile in a WSI. The scale bar for the WSI denotes the length corresponding to 5 mm. Features are computed at 3 scales using tile sizes shown in red, purple, and black (small, medium, large tiles respectively) outlines. The scale bar denotes the length corresponding to 256 μm. **b**, For each feature, the distribution of values across tiles is computed. The decile values for each feature's CDF, concatenated across features and scales, form the WSI representation.

flexibility in capturing morphological information at different scales. We employ Inception*V3 pre-trained on ImageNet as a backbone to generate a representation for each tile-tile in a 2048-dimensional feature space (Fig. 1a). Next, we encode each feature at the slide-level by specifying its decile distribution across tiles, i.e., for each feature at each tile size, we report the value at which the cumulative distribution function (CDF) reaches the respective decile (Fig. 1b). Thus, SAMPLER represents each WSI by a 1 × 10 × 2048 = 61,440-dimensional feature vector. The WSI feature vector can then be used for downstream analysis.

Effectiveness of SAMPLER for cancer subtype classification

To evaluate the effectiveness of SAMPLER, we examined its performance on several subtype classification tasks with a range of difficulties: distinguishing invasive ductal carcinoma (IDC) from invasive lobular carcinoma

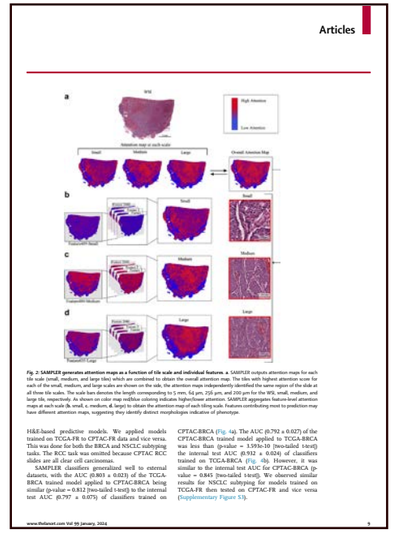

Fig. 2: SAMPLER generates attention maps as a function of tile scale and individual features. a, SAMPLER outputs attention maps for each tile scale (small, medium, and large tiles) which are combined to obtain the overall attention map. The tiles with highest attention score for each of the small, medium, and large scales are shown on the side, the attention maps independently identified the same region of the slide at all three tile scales. The scale bars denotes the length corresponding to 5 mm, 64 μm, 256 μm, and 1000 μm for the WSI, small, medium, and large tile, respectively. As shown on color map red/blue coloring indicates higher/lower attention. SAMPLER aggregates feature-level attention maps at each scale (**b**, small, **c**, medium, **d**, large) to obtain the attention map of each tiling scale. Features contributing most to prediction may have different attention maps, suggesting they identify distinct morphologies indicative of phenotype.

H&E-based predictive models. We applied models trained on TCGA-FR to CPTAC-FR data and vice versa. This was done for both the BRCA and NSCLC subtyping tasks. The RCC task was omitted because CPTAC RCC slides are all clear cell carcinomas.

SAMPLER classifiers generalized well to external datasets, with the AUC (0.803 ± 0.023) of the TCGA-BRCA trained model applied to CPTAC-BRCA being similar (p-value = 0.812 [two-tailed t-test]) to the internal test AUC (0.797 ± 0.075) of classifiers trained on CPTAC-BRCA (Fig. 4a). The AUC (0.792 ± 0.027) of the CPTAC-BRCA trained model applied to TCGA-BRCA was less than (p-value = 3.593e-10 [two-tailed t-test]) the internal test AUC (0.932 ± 0.024) of classifiers trained on TCGA-BRCA (Fig. 4b). However, it was similar to the internal test AUC for CPTAC-BRCA (p-value = 0.845 [two-tailed t-test]). We observed similar results for NSCLC subtyping for models trained on TCGA-FR then tested on CPTAC-FR and vice versa (Supplementary Figure S3).

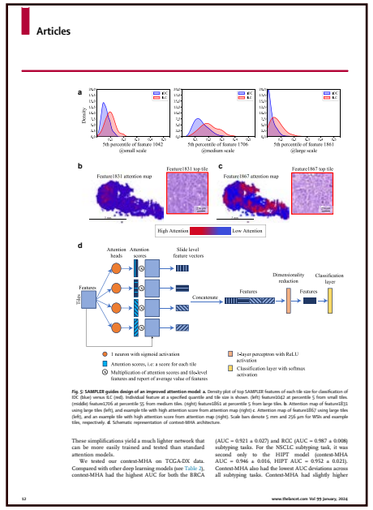

Fig. 3: SAMPLER guides design of an improved attention model. a, Density plot of top SAMPLER features of each tile size for classification of IDC (blue) versus ILC (red). Individual feature at a specified quantile and tile size is shown. (left) feature1042 at percentile 5 from small tiles, (middle) feature1706 at percentile 15 from medium tiles, (right) feature1861 at percentile 5 from large tiles. **b**, Attention map of feature1831 using large tiles (left), and example tile with high attention score from attention map (right). **c**, Attention map of feature1867 using large tiles (left), and an example tile with high attention score from attention map (right). Scale bars denote 5 mm and 250 μm for WSIs and example tiles, respectively. **d**, Schematic representation of context-MHA architecture.

These simplifications yield a much lighter network that can be more easily trained and tested than standard attention models.

We tested our context-MHA on TCGA-DX data. Compared with other deep learning models (see Table 2), context-MHA had the highest AUC for both the BRCA (AUC = 0.921 ± 0.027) and RCC (AUC = 0.987 ± 0.008) subtyping tasks. For the NSCLC subtyping task, it was second only to the HIPT model (context-MHA AUC = 0.946 ± 0.014, HIPT AUC = 0.952 ± 0.021). Context-MHA also had the lowest AUC deviations across all subtyping tasks. Context-MHA had slightly higher

SAMPLER: unsupervised representations for rapid analysis of whole slide tissue images

Client: The Jackson Laboratory
Year: 2023
Software: Adobe Illustrator

Microscale Fluid Dynamics: Coulomb Explosion Series

Client: KAUST
Year: 2024
Software: Cinema 4D - Adobe Photoshop

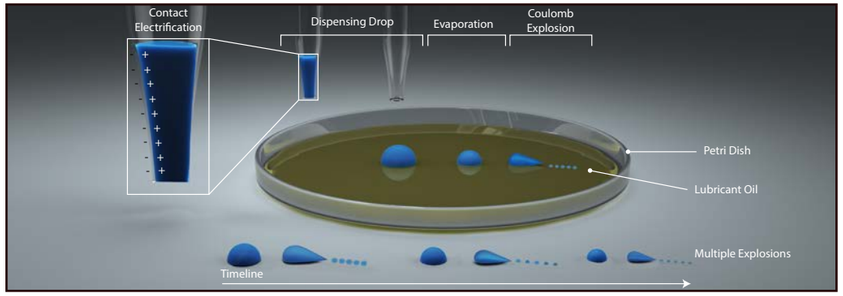

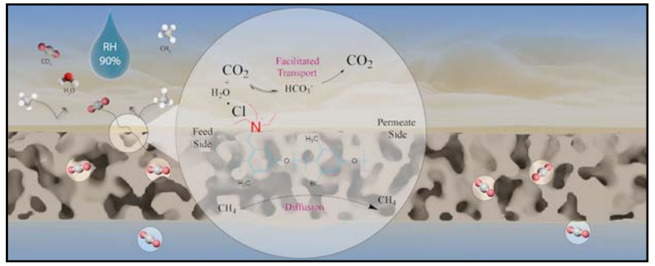

Quaternary ammonium-functionalized membranes enhance gas separation, especially in high humidity

Client:KAUST
Year: 2024
Software: Cinema 4D - Adobe Photoshop

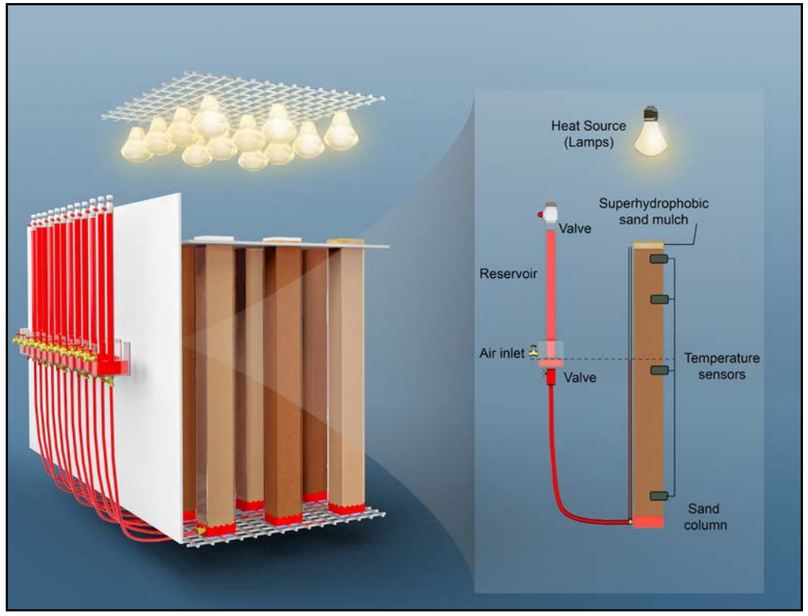

SandX: A Nature-Based Water Conservation Technology for Boosting Agriculture

Client:KAUST
Year: 2024
Software: Cinema 4D - Adobe Photoshop

DNA–protein hybrid nanostructures self-assemble via histone–DNA interactions

Client: KAUST
Year: 2024
Software: Cinema 4D - Adobe Photoshop

From Rough Sketch to Rendered Figure

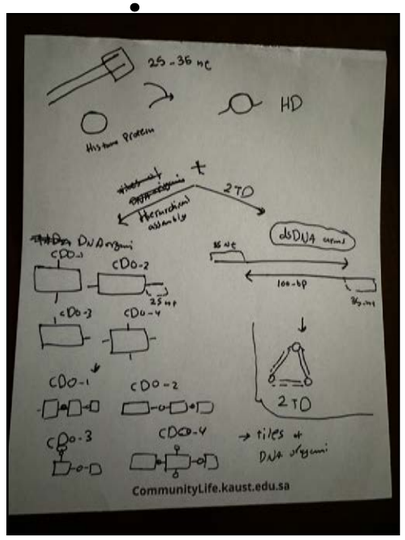

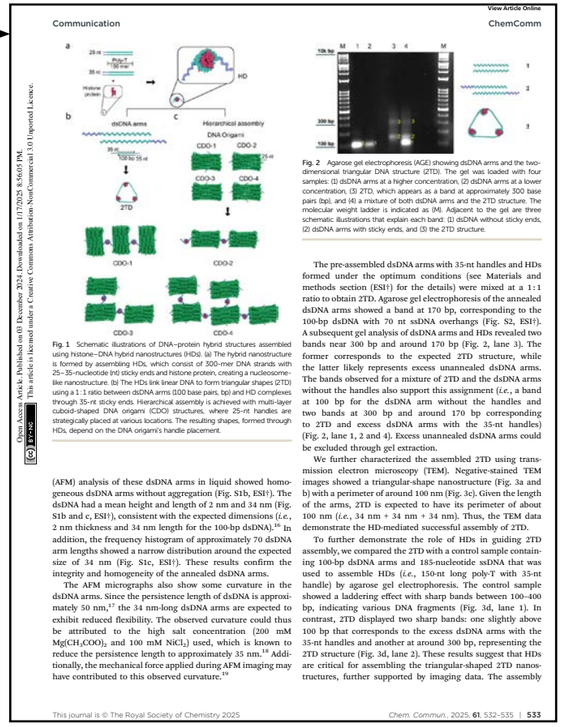

View Article Online
Communication
ChemComm

Open Access Article. Published on 03 December 2024. Downloaded on 1/17/2025 8:56:05 PM.
This article is licensed under a Creative Commons Attribution-NonCommercial 3.0 Unported Licence.

Fig. 1 Schematic illustrations of DNA–protein hybrid structures assembled using histone–DNA hybrid nanostructures (HDs). (a) The hybrid nanostructure is formed by assembling HDs, which consist of 300-mer DNA strands with 25–35-nucleotide (nt) sticky ends and histone protein, creating a nucleosome-like nanostructure. (b) The HDs link linear DNA to form triangular shapes (2TD) using a 1 : 1 ratio between dsDNA arms (100 base pairs, bp) and HD complexes through 35-nt sticky ends. Hierarchical assembly is achieved with multi-layer cuboid-shaped DNA origami (CDO) structures, where 25-nt handles are strategically placed at various locations. The resulting shapes, formed through HDs, depend on the DNA origami's handle placement.

Fig. 2 Agarose gel electrophoresis (AGE) showing dsDNA arms and the two-dimensional triangular DNA structure (2TD). The gel was loaded with four samples: (1) dsDNA arms at a higher concentration, (2) dsDNA arms at a lower concentration, (3) 2TD, which appears as a band at approximately 300 base pairs (bp), and (4) a mixture of both dsDNA arms and the 2TD structure. The molecular weight ladder is indicated as (M). Adjacent to the gel are three schematic illustrations that explain each band: (1) dsDNA without sticky ends, (2) dsDNA arms with sticky ends, and (3) the 2TD structure.

(AFM) analysis of these dsDNA arms in liquid showed homogeneous dsDNA arms without aggregation (Fig. S1b, ESI†). The dsDNA had a mean height and length of 2 nm and 34 nm (Fig. S1b and c, ESI†), consistent with the expected dimensions (*i.e.*, 2 nm thickness and 34 nm length for the 100-bp dsDNA).[16] In addition, the frequency histogram of approximately 70 dsDNA arm lengths showed a narrow distribution around the expected size of 34 nm (Fig. S1c, ESI†). These results confirm the integrity and homogeneity of the annealed dsDNA arms.

The AFM micrographs also show some curvature in the dsDNA arms. Since the persistence length of dsDNA is approximately 50 nm,[17] the 34 nm-long dsDNA arms are expected to exhibit reduced flexibility. The observed curvature could thus be attributed to the high salt concentration (200 mM $Mg(CH_3COO)_2$ and 100 mM $NiCl_2$) used, which is known to reduce the persistence length to approximately 35 nm.[18] Additionally, the mechanical force applied during AFM imaging may have contributed to this observed curvature.[19]

The pre-assembled dsDNA arms with 35-nt handles and HDs formed under the optimum conditions (see Materials and methods section (ESI†) for the details) were mixed at a 1 : 1 ratio to obtain 2TD. Agarose gel electrophoresis of the annealed dsDNA arms showed a band at 170 bp, corresponding to the 100-bp dsDNA with 70 nt ssDNA overhangs (Fig. S2, ESI†). A subsequent gel analysis of dsDNA arms and HDs revealed two bands near 300 bp and around 170 bp (Fig. 2, lane 3). The former corresponds to the expected 2TD structure, while the latter likely represents excess unannealed dsDNA arms. The bands observed for a mixture of 2TD and the dsDNA arms without the handles also support this assignment (*i.e.*, a band at 100 bp for the dsDNA arm without the handles and two bands at 300 bp and around 170 bp corresponding to 2TD and excess dsDNA arms with the 35-nt handles) (Fig. 2, lane 1, 2 and 4). Excess unannealed dsDNA arms could be excluded through gel extraction.

We further characterized the assembled 2TD using transmission electron microscopy (TEM). Negative-stained TEM images showed a triangular-shape nanostructure (Fig. 3a and b) with a perimeter of around 100 nm (Fig. 3c). Given the length of the arms, 2TD is expected to have its perimeter of about 100 nm (*i.e.*, 34 nm + 34 nm + 34 nm). Thus, the TEM data demonstrate the HD-mediated successful assembly of 2TD.

To further demonstrate the role of HDs in guiding 2TD assembly, we compared the 2TD with a control sample containing 100-bp dsDNA arms and 185-nucleotide ssDNA that was used to assemble HDs (*i.e.*, 150-nt long poly-T with 35-nt handle) by agarose gel electrophoresis. The control sample showed a laddering effect with sharp bands between 100–400 bp, indicating various DNA fragments (Fig. 3d, lane 1). In contrast, 2TD displayed two sharp bands: one slightly above 100 bp that corresponds to the excess dsDNA arms with the 35-nt handles and another at around 300 bp, representing the 2TD structure (Fig. 3d, lane 2). These results suggest that HDs are critical for assembling the triangular-shaped 2TD nanostructures, further supported by imaging data. The assembly

This journal is © The Royal Society of Chemistry 2025

From Rough Sketch and Raw Manuscript to Rendered Figure

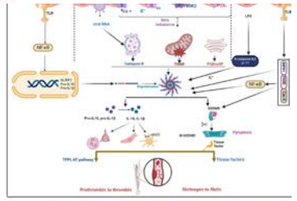

Figure 2: Schematic mechanisms of NLRP3 inflammasome activation. NLRP by various endogenous dangerous associated molecular patterns (DAMPs) a associated molecular patterns (PAMPs). In canonical NLRP3 inflammasome, due disbalances, could show the affect on mitochondria, lysosomes, golgi body. numerous mediators which could be released mtROS, cathepsin B etc. components, including NLRP3, ASC, and procaspase-1, form the NLRP3 complexes. Finally, activated caspase-1 induces the inflammatory form of cell de pyroptosis and cleaves the precursor cytokines pro-IL-1β and pro-IL-18, g biologically active cytokines IL-1β and IL-18. Non-canonical NLRP3 inflammasom activated by cytosolic LPS sensing by caspase 4/5/11 and then they cut th

Functional Roles of the Inflammasome Complexes in Deep Vein Thrombosis

Client: Life Science Editors
Year: 2024
Software: Adobe Illustrator

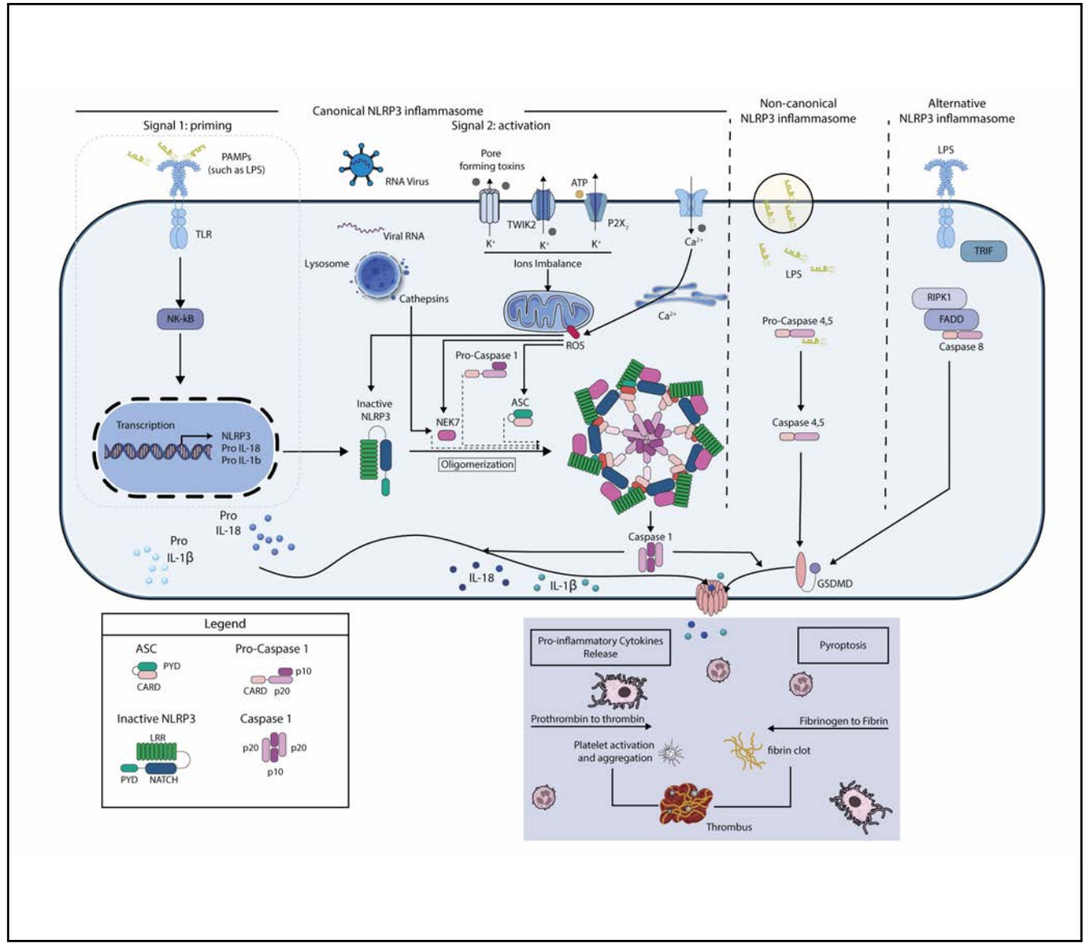

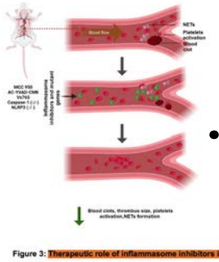

Figure 3: Therapeutic role of inflammasome inhibitors in DVT

From Rough Sketch and Raw Manuscript to Rendered Figure

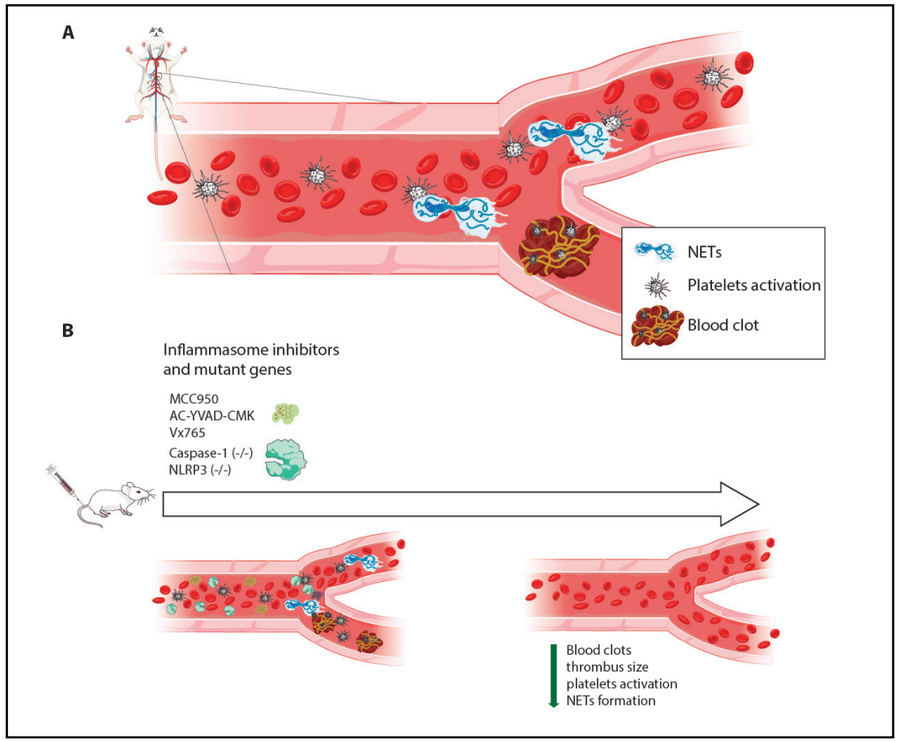

From Rough Sketch to Rendered Figure

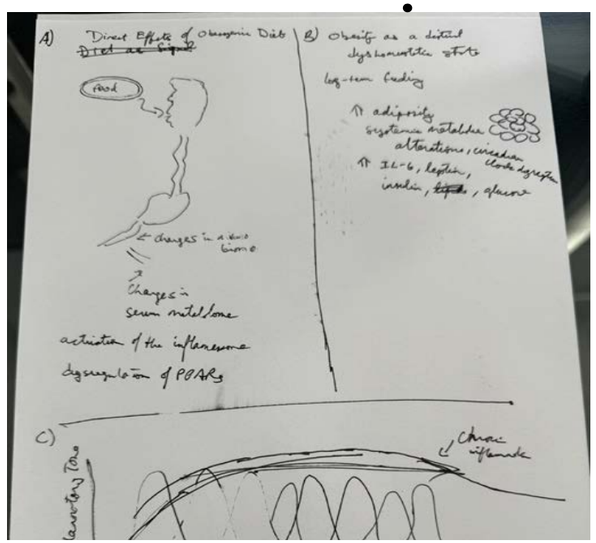

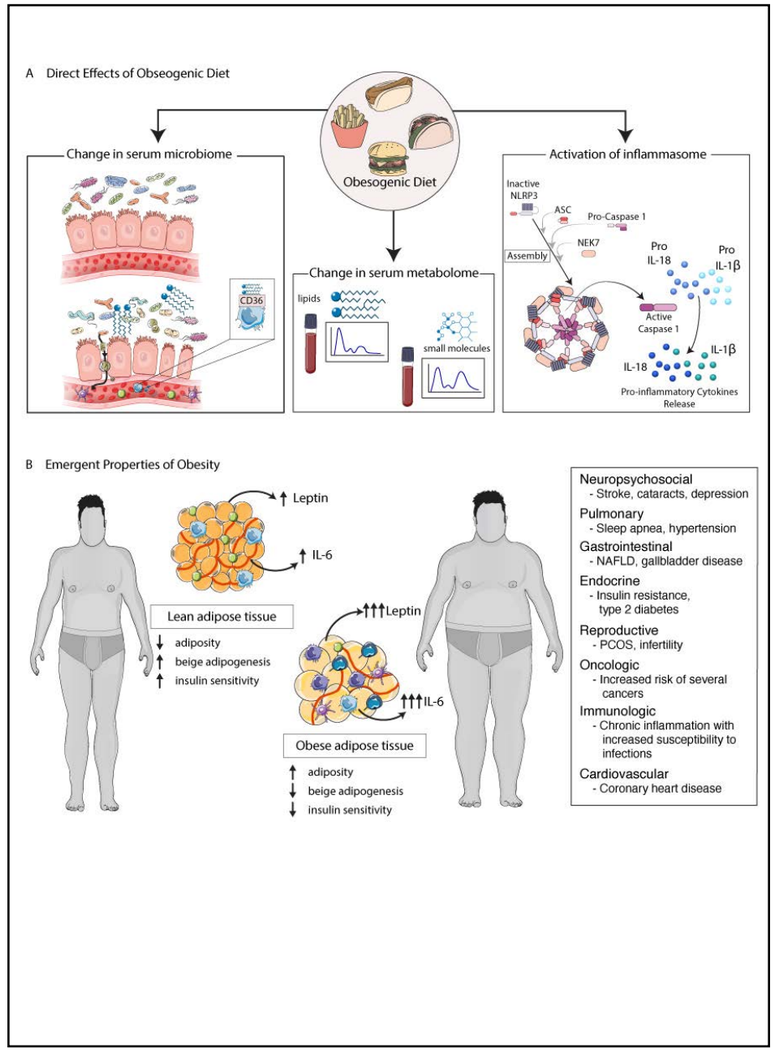

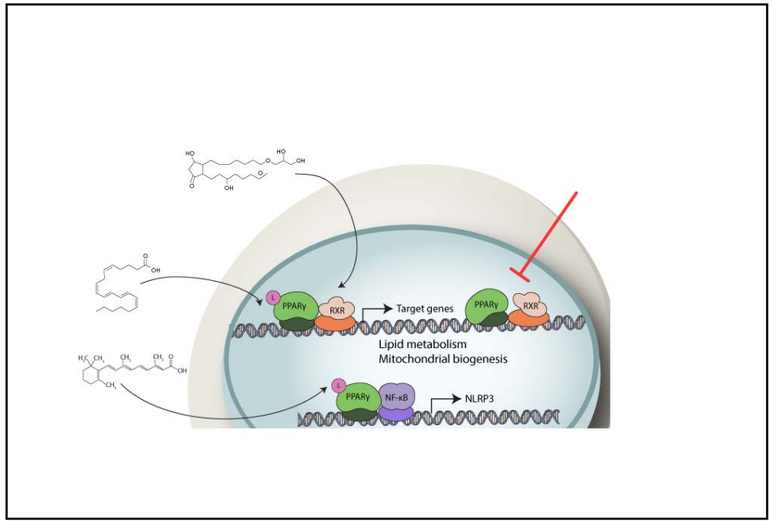

Obesity alters pathology and treatment response in inflammatory disease

Client: Life Science Editors
Year: 2024
Software: Adobe Illustrator

GRANT PROPOSAL SUMMARIES

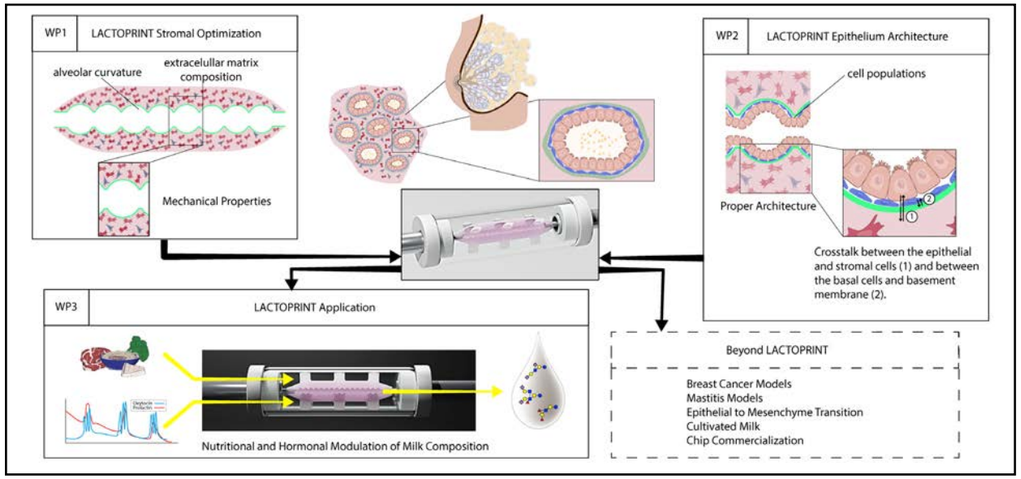

Graphical Abstract for NIH Grant

Client: Life Science Editors
Year: 2024
Software: Adobe Illustrator

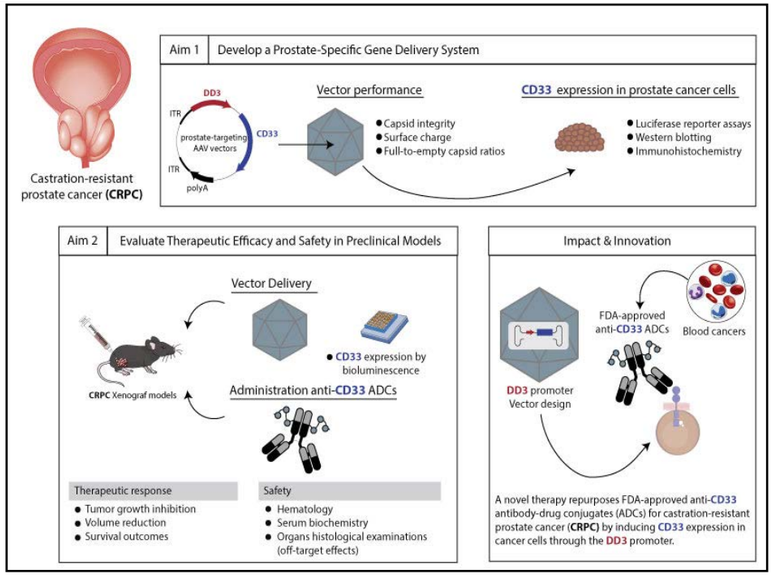

Graphical Abstract for Grant-Lactoprint

Client: Life Science Editors-
Year: 2024
Software: Adobe Illustrator

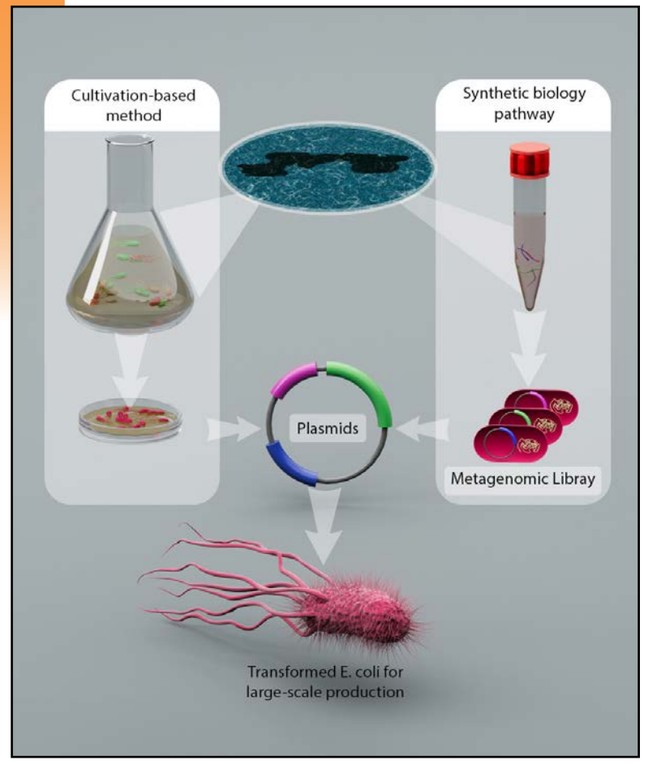

Graphical Abstract for several Grants

Client: Chicago University
Year: 2024
Software: Cinema 4D - Adobe Photoshop - Adobe Illustrator

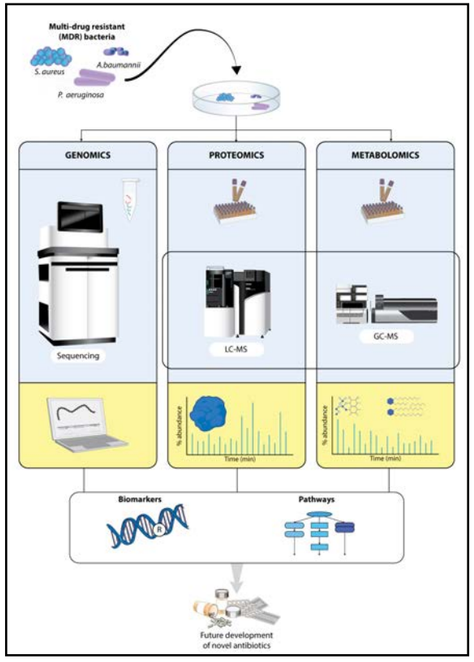

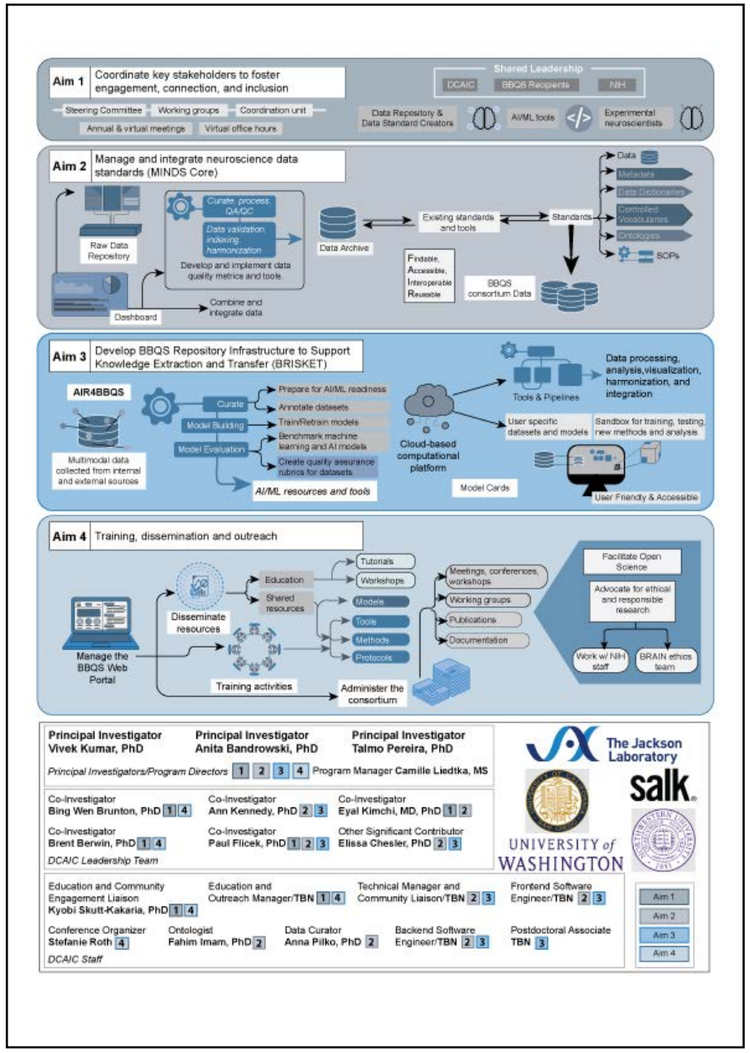

Graphical Abstract for Grant - DCAIC

Client: The Jackson Laboratory
Year: 2023
Software: Adobe Illustrator

INFOGRAPHICS DESIGN

Antisense oligonucleotides

Client: TechNOA, Singapore
Year: 2019
Software: AutoDesk Maya - Adobe Photoshop - Adobe Illustrator

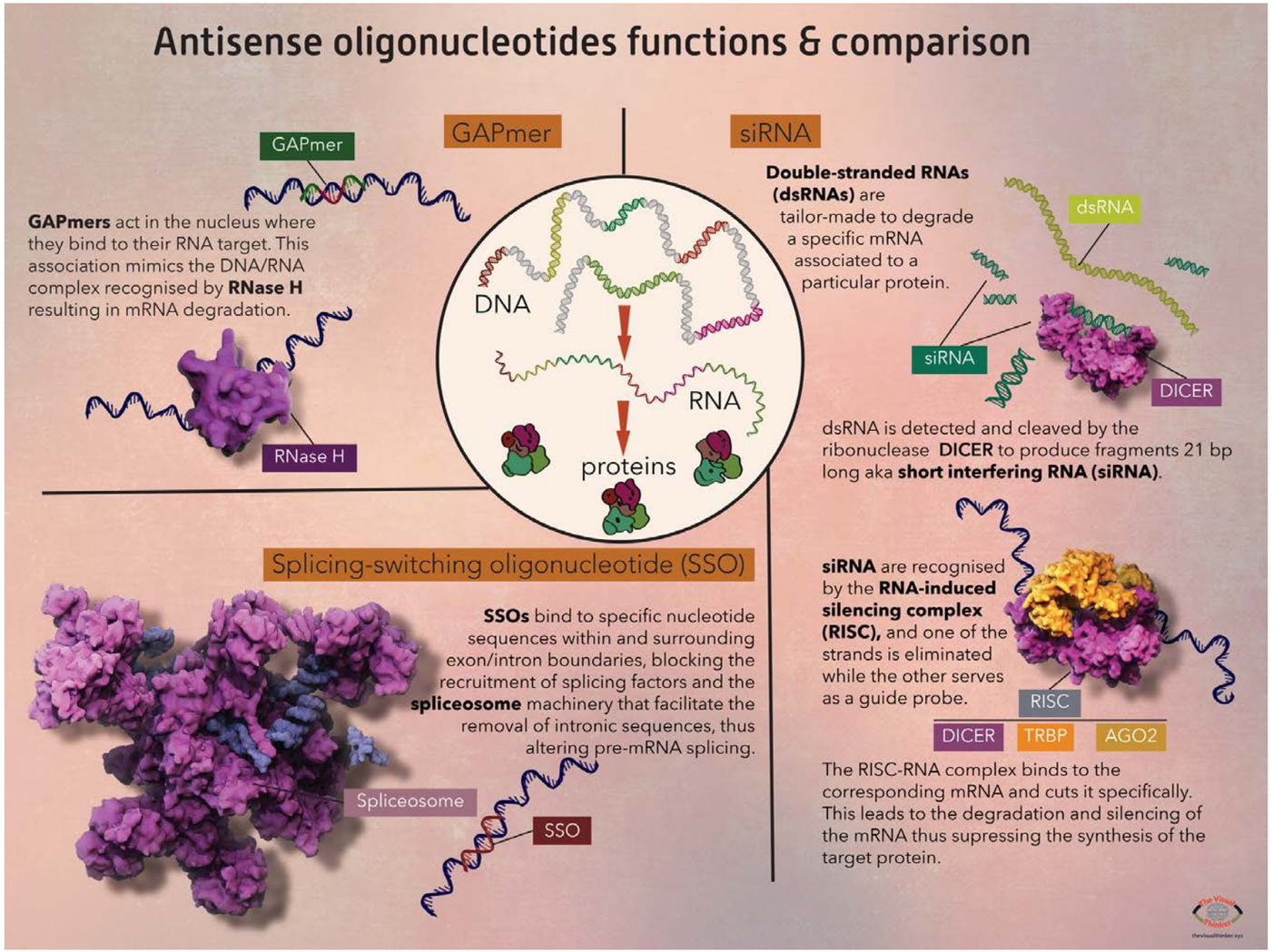

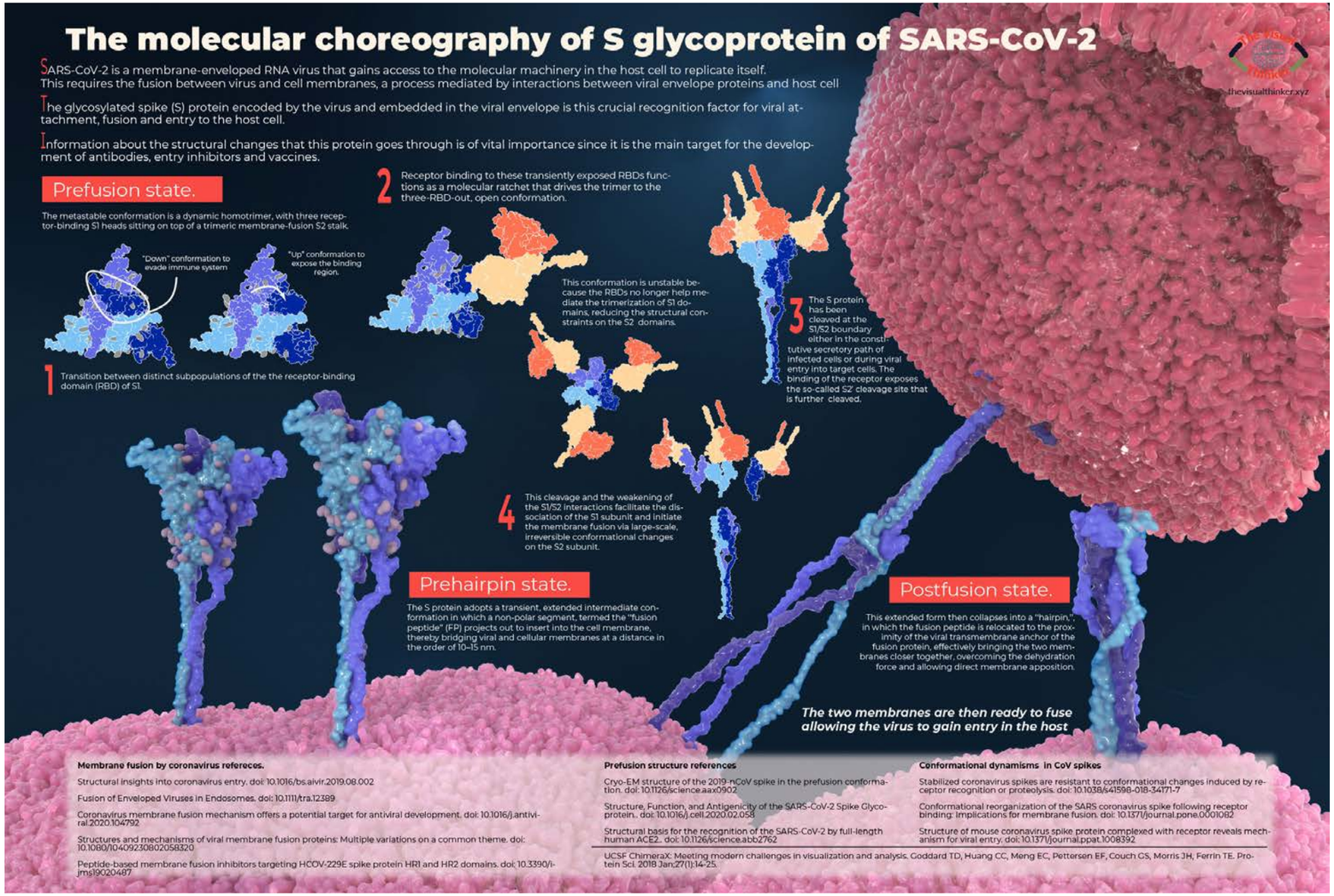

SARS-2: Spike protein accesing the human cell and Viron structure

Client: Academia Sinica, TW
Year: 2022
Software: AutoDesk Maya - Adobe Photoshop

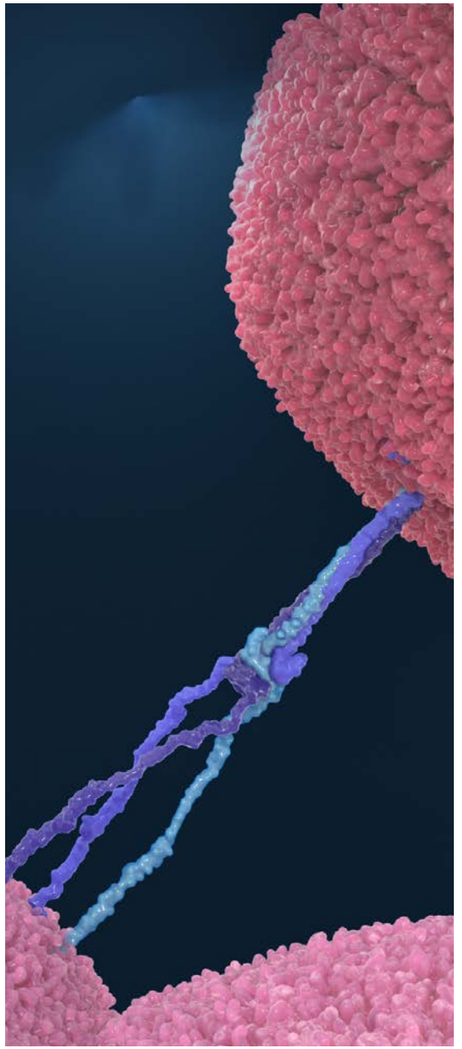

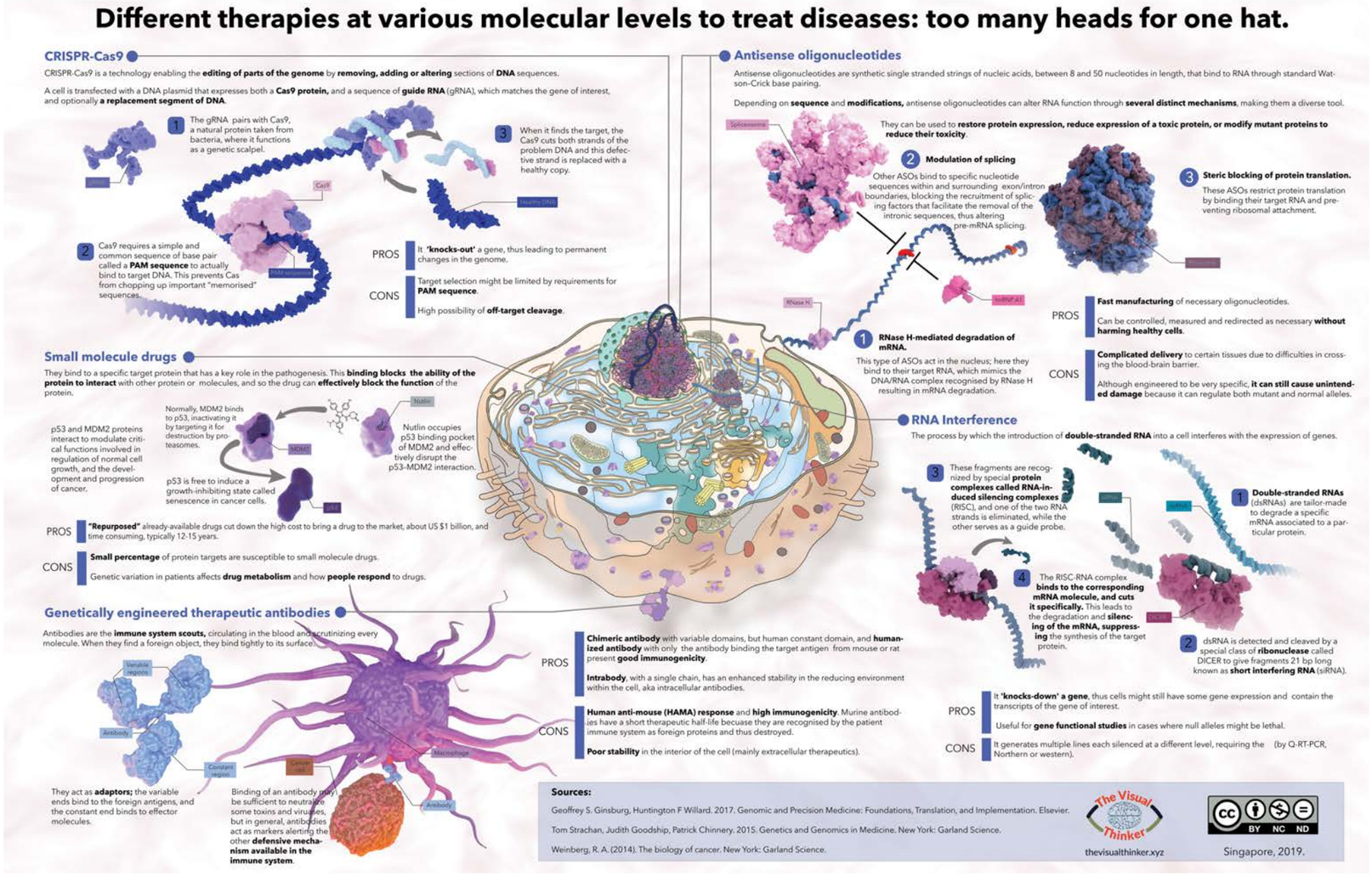

Different molecular therapies

Client: Personal project
Year: 2019
Software: AutoDesk Maya - Adobe Photoshop - Adobe Illustrator

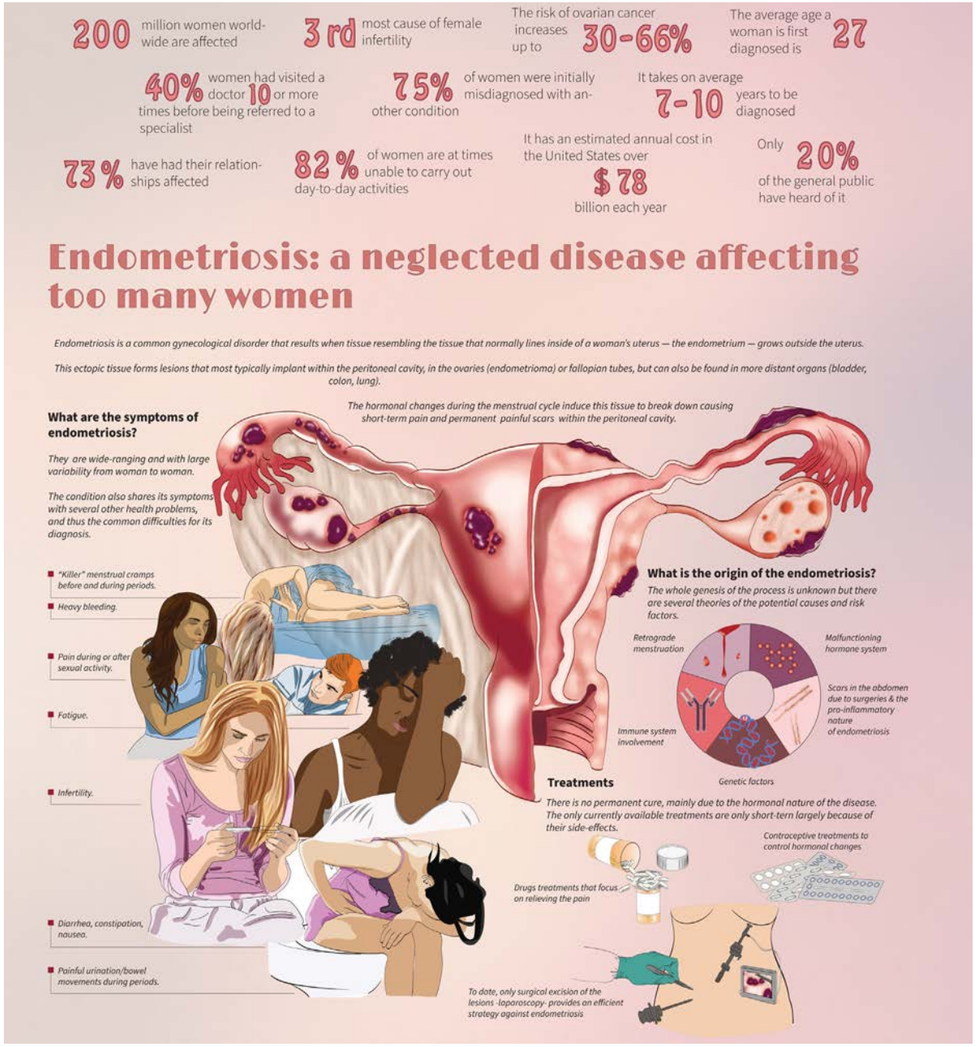

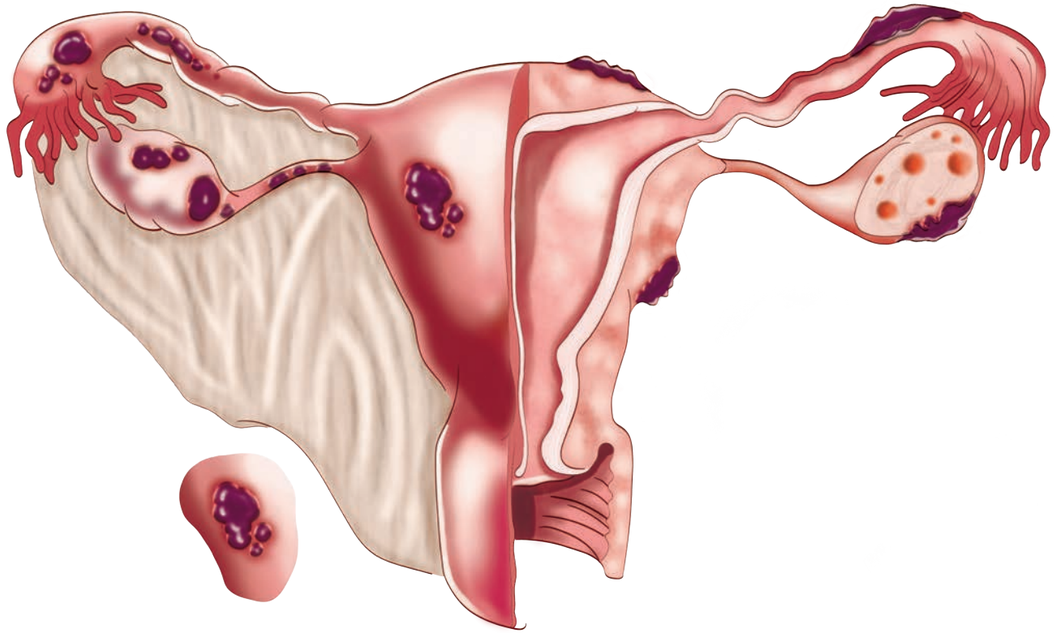

Endometriosis: a neglegted disease

Client: The Jackson Laboratory, USA
Year: 2021
Software: Adobe Photoshop - Adobe Illustrator

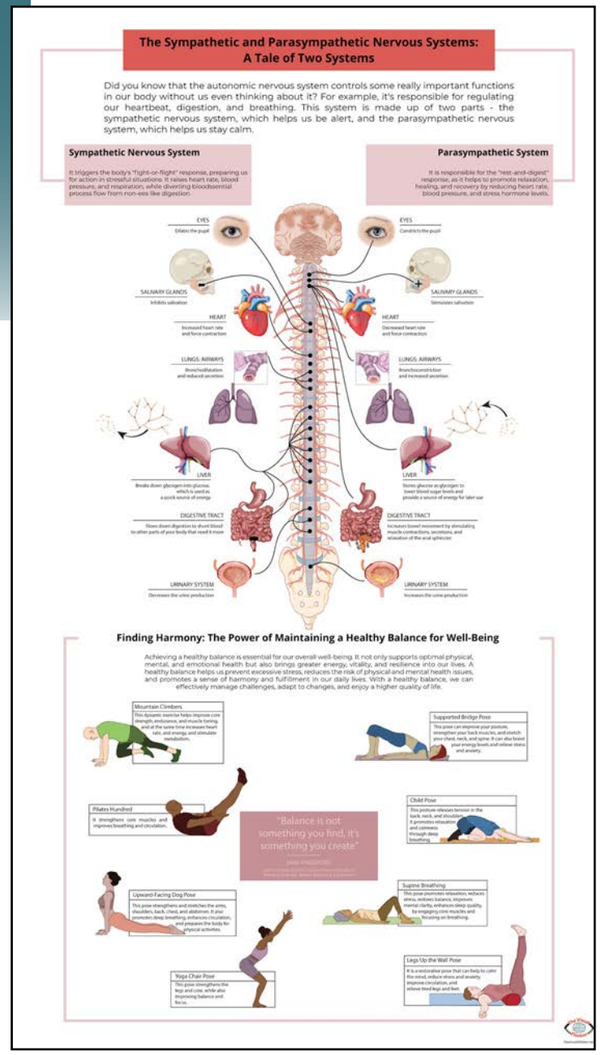

Nervous Systems and Pilates

Client: Private Pilates Studio
Year: 2023
Software: Adobe Photoshop - Adobe Illustrator

Pre-Diabetes

Client: Personal project for the Series: Science in Everywhere
Year: 2023
Software: Adobe Photoshop

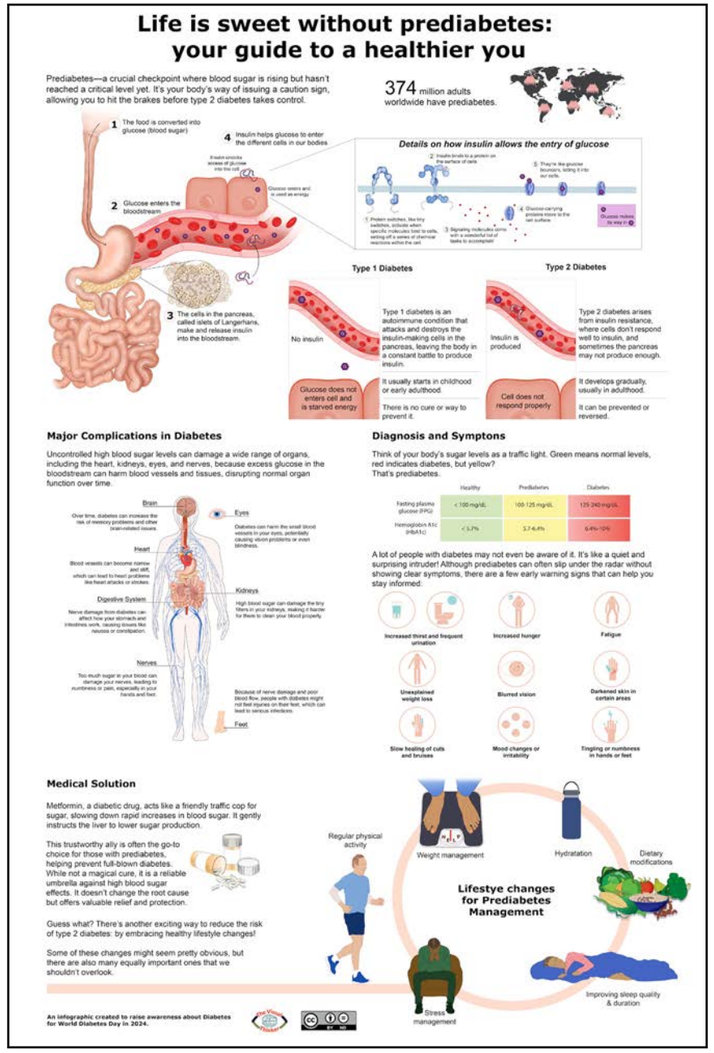

Glaucoma

Client: Personal project for the Series: Science in Everywhere
Year: 2023
Software: Adobe Photoshop

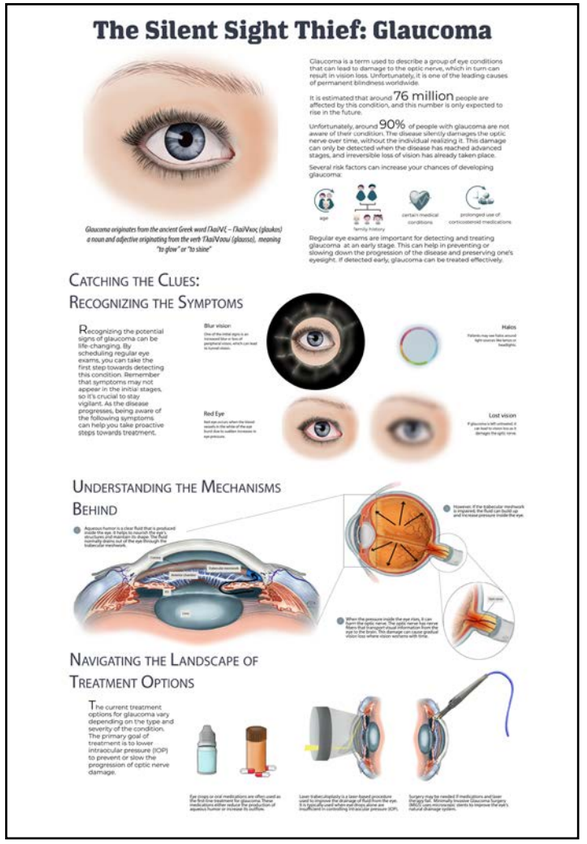

EDITORIAL WORK

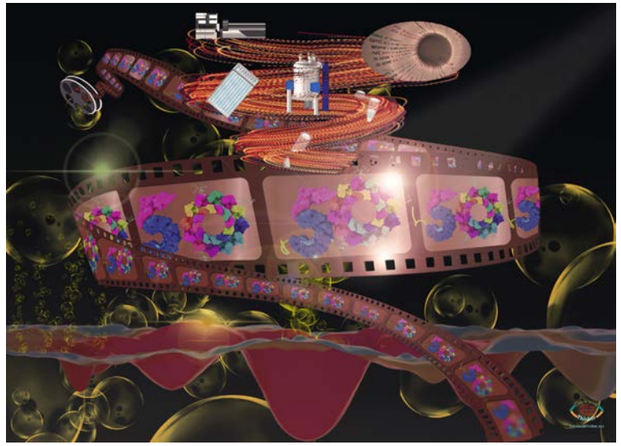

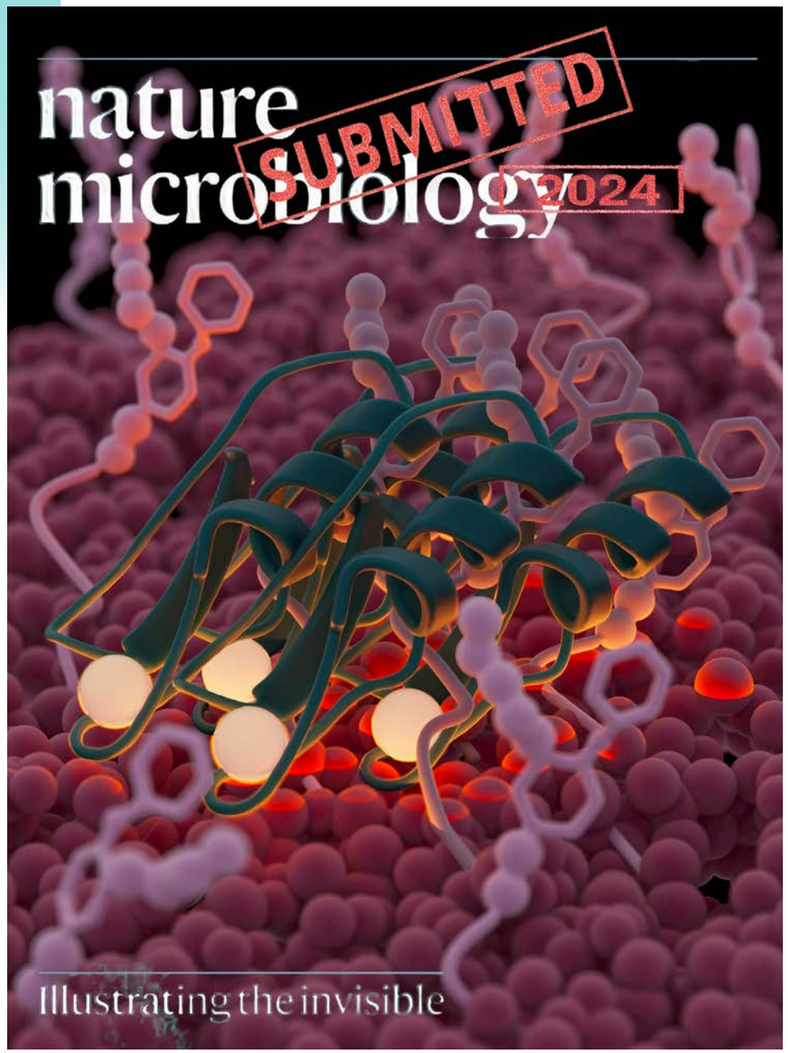
nature microbiology
SUBMITTED
2024
Illustrating the invisible


nature cancer
SUBMITTED
2024


bleed
trim
live area
interior alignment
SUBMITTED
2024
Molecular Cell
Volume XX
Number XX
Month XX, 2022
center
Left Headline
Goes Here
CellPress

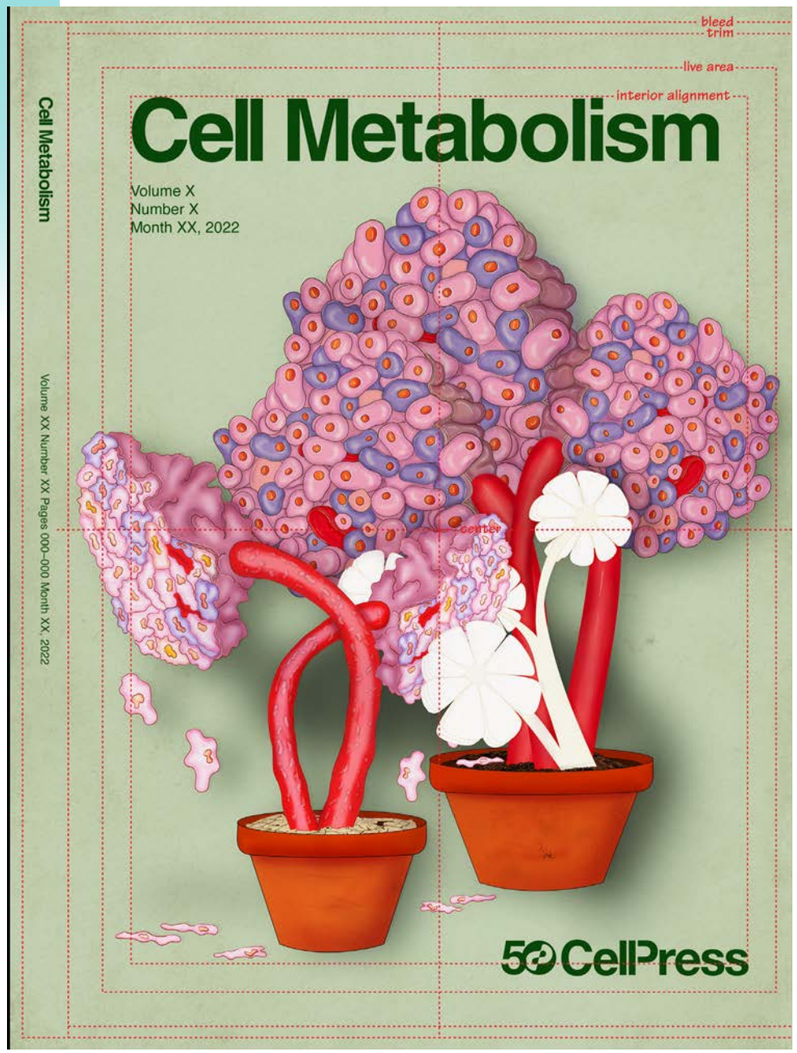
bleed
trim
live area
interior alignment
Cell Metabolism
Volume X
Number X
Month XX, 2022
center
Cell Metabolism
Volume XX Number XX Pages 000–000 Month XX, 2022
CellPress


Science
AAAS
SUBMITTED
2024


nature genetics
SUBMITTED
2024

3D MODELS & ILLUSTRATION

Bacteria morphology studies

Client: Agency for Science, Technology and Research, Singapore
Year: 2021
Software: AutoDesk Maya - Zbrush - Adobe Photoshop

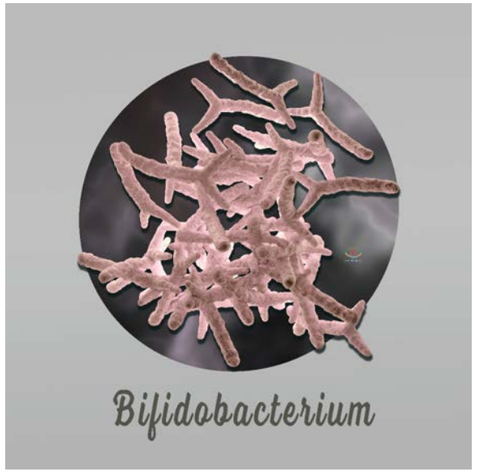

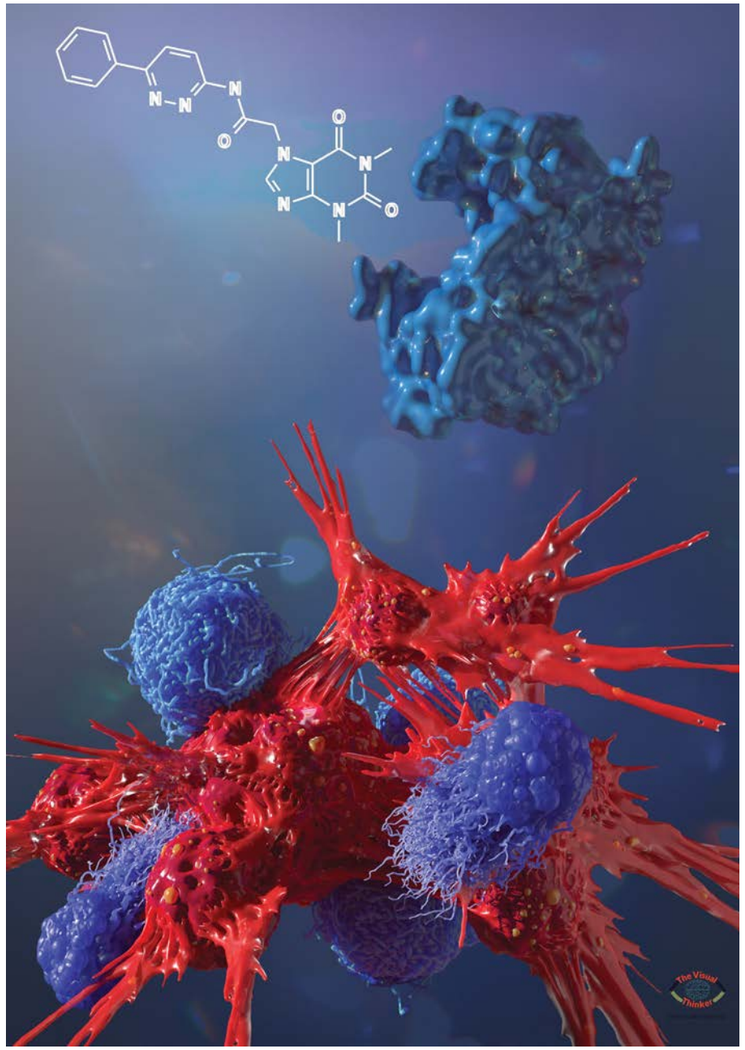

A*STAR@30: 30 Innovations and inventions over three decades

Client: Agency for Science, Technology and Research, Singapore
Year: 2021
Software: AutoDesk Maya - Adobe Photoshop

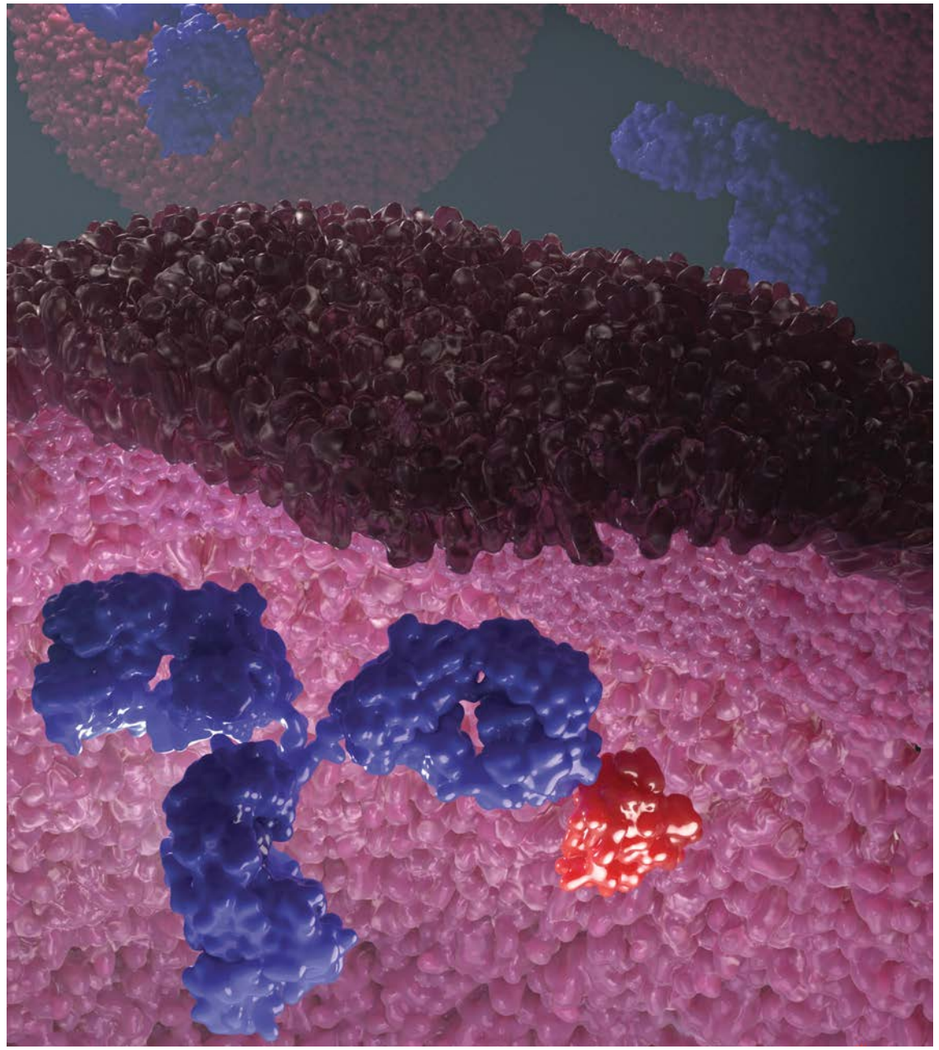

SARS-2: Spike protein accesing the human cell and Viron structure

Client: Personal project
Year: 2021
Software: AutoDesk Maya - Adobe Photoshop

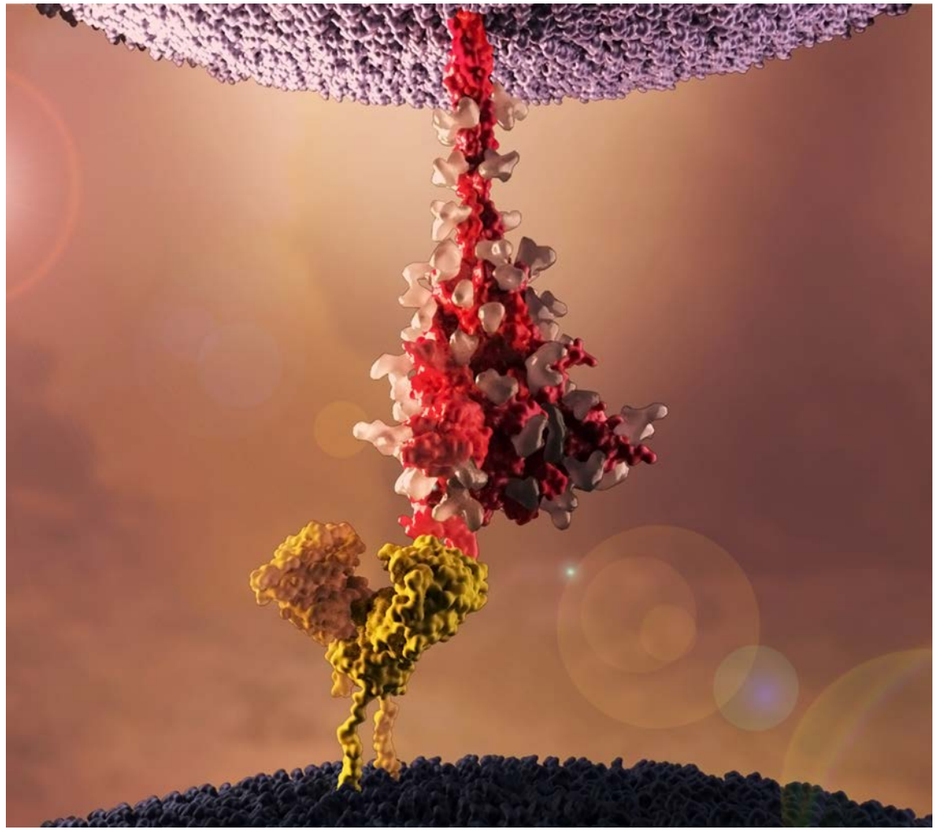

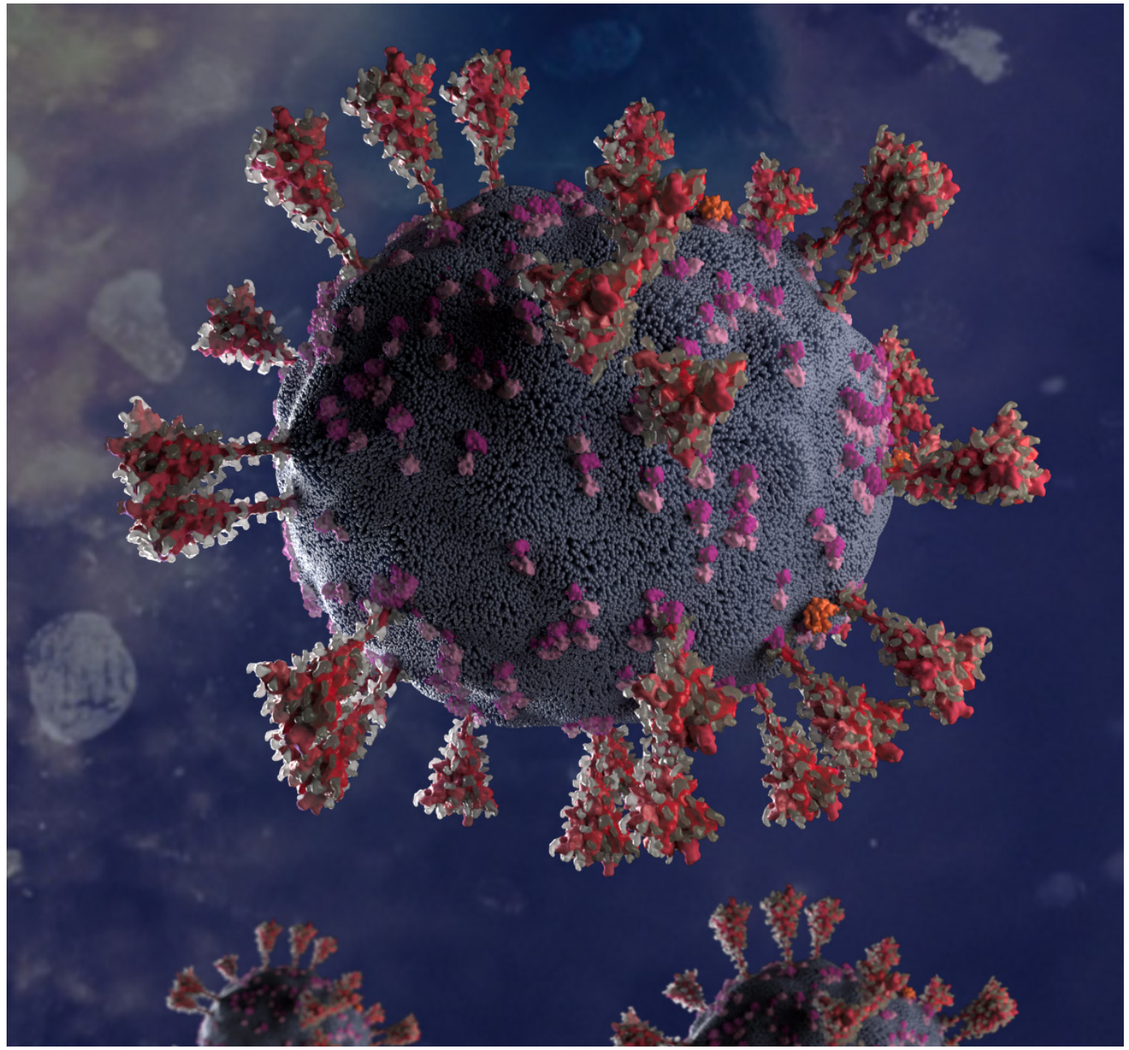

thevisualthinker.xyz